



HAL
open science

Acoustical properties of air-saturated porous material with periodically distributed dead-end pores

Philippe Leclaire, Olga Umnova, Thomas Dupont, Raymond Panneton

► To cite this version:

Philippe Leclaire, Olga Umnova, Thomas Dupont, Raymond Panneton. Acoustical properties of air-saturated porous material with periodically distributed dead-end pores. *Journal of the Acoustical Society of America*, 2015, 134 (4), pp.1772-1782. 10.1121/1.4916712 . hal-01323687

HAL Id: hal-01323687

<https://hal.science/hal-01323687>

Submitted on 1 Jun 2016

HAL is a multi-disciplinary open access archive for the deposit and dissemination of scientific research documents, whether they are published or not. The documents may come from teaching and research institutions in France or abroad, or from public or private research centers.

L'archive ouverte pluridisciplinaire **HAL**, est destinée au dépôt et à la diffusion de documents scientifiques de niveau recherche, publiés ou non, émanant des établissements d'enseignement et de recherche français ou étrangers, des laboratoires publics ou privés.



Distributed under a Creative Commons Attribution 4.0 International License

Acoustical properties of air-saturated porous material with periodically distributed dead-end pores^{a)}

P. Leclaire^{b)}

DRIVE-ISAT, Université de Bourgogne, 49 Rue Mademoiselle Bourgeois, 58027 Nevers Cedex, France

O. Umnova

Acoustics Research Centre, University of Salford, Salford M5 4WT, United Kingdom

T. Dupont

DRIVE-ISAT, Université de Bourgogne, 49 Rue Mademoiselle Bourgeois, 58027 Nevers Cedex, France

R. Panneton

GAUS, Université de Sherbrooke, Sherbrooke, Québec J1K 2R1, Canada

(Received 26 October 2014; revised 9 March 2015; accepted 23 March 2015)

A theoretical and numerical study of the sound propagation in air-saturated porous media with straight main pores bearing lateral cavities (dead-ends) is presented. The lateral cavities are located at “nodes” periodically spaced along each main pore. The effect of periodicity in the distribution of the lateral cavities is studied, and the low frequency limit valid for the closely spaced dead-ends is considered separately. It is shown that the absorption coefficient and transmission loss are influenced by the viscous and thermal losses in the main pores as well as their perforation rate. The presence of long or short dead-ends significantly alters the acoustical properties of the material and can increase significantly the absorption at low frequencies (a few hundred hertz). These depend strongly on the geometry (diameter and length) of the dead-ends, on their number per node, and on the periodicity along the propagation axis. These effects are primarily due to low sound speed in the main pores and to thermal losses in the dead-end pores. The model predictions are compared with experimental results. Possible designs of materials of a few cm thicknesses displaying enhanced low frequency absorption at a few hundred hertz are proposed.

I. INTRODUCTION

Air-saturated porous materials are most efficient for noise reduction applications if the characteristic sizes of the pores or of the interparticle spaces are on the order of the viscous and thermal boundary layer thicknesses. At audible frequencies, the order of magnitude of the characteristic sizes ranges from a few hundred micrometers to a few millimeters. The pores should also be interconnected and opened to the surroundings. The models developed over the years are able to predict accurately the acoustic behavior of highly porous absorbing materials such as for instance reticulated polyurethane foams or fibrous materials.¹ It was shown more recently that these models are not accurate enough to properly describe the acoustic properties of other materials that can contain partially opened or dead-end pores. Dead-end pores are closed at one end so that fluid flow does not take place in all the pores of the medium. A model capable of accounting for this feature was recently developed and used to successfully describe the acoustical properties of materials with lower porosity such as metallic foams and those with

surface dead-end pores.² It was found that the presence of dead-ends had the effect of increasing the absorption coefficient at frequencies controlled by the average length of the dead-ends. This motivates the present study. Structured materials with well-controlled microgeometry including dead-end pores can be designed and fabricated by making use of recent technologies such as precision machining or three-dimensional (3D) printing. The designed materials slab could contain, for example, circular perforations. Some of the perforations should go in through the thickness of the layer while others should end inside it to create dead-end pores.

The present contribution is concerned with the theoretical and numerical study of a structured perforated material containing periodically spaced dead-end pores. Waves propagating in periodic structures are known as “Bloch waves.” Examples of such structures are ducts with periodically distributed lateral cavities or resonators (see Refs. 3–5, for example). The periodicity introduces frequency stop bands, i.e., frequency intervals where no propagating waves are supported by the structure. Most studies deal with the situation where the structure period is on the order of the wavelength to observe the stop bands (example, sonic crystals). The distances between the perforations and dead-ends considered in the present study are about 1 cm or less. Therefore the wavelengths on the order of the period correspond to frequencies above 10 kHz. However, the stop bands due to

resonances of the lateral dead-ends are also predicted at low frequencies, typically a few hundred hertz, much lower than the frequencies corresponding to the period. This constitutes the central originality of the present contribution. The dead-end pores considered here are simple closed cavities. However, the model can account for more complex geometries including Helmholtz resonators. The aim of this work is to extend the model for the acoustical properties of porous materials with dead-end porosity developed earlier² to account for periodicity in the spatial distribution of dead-ends within the thickness of the material. The model presented here provides a simple tool for optimizing the material inner structure to achieve the desired acoustical properties.

The paper is organized as follows: In Sec. II, a dispersion relationship for waves propagating in the channel (called main pore in the following) with periodically distributed side branches³ is recalled and extended to account for the multiple side branches (called dead-end pores in the following) at one node. The transfer matrix method (TMM) is then developed to predict absorption and transmission characteristics of the finite thickness material slab with dead-end porosity. In Sec. III, the low frequency limit of the model is investigated when the distance between neighboring dead-end pores is small compared to the wavelength of sound in the main pore. Simple expressions for the dynamic density and compressibility are derived. The limitations of the model are established by comparing its predictions with the transfer matrix approach developed in Sec. II. In Sec. IV, the effect of the dead-ends on the behavior of a single main pore is investigated and the limitations of the low frequency approximation are discussed by comparing its prediction with those of the TMM. In Sec. V, the model is validated by comparing its predictions for the absorption coefficient of the material slab with FEM simulations. Experimental results on samples obtained from 3D printing are also presented and compared with the model. In Sec. VI, possible designs of perforated materials with lateral dead-ends featuring improved absorption at low frequencies are suggested. Their absorption properties are simulated using the models developed. The main findings are summarized in the final section.

II. SOUND PROPAGATION IN THE MATERIAL WITH PERIODICALLY DISTRIBUTED DEAD-END PORES—FULL ANALYTICAL TMM MODEL

In the previous study (Ref. 2), no interactions between the dead-ends were taken into account either for the metallic foams with randomly distributed dead-ends or for the structured material with surface dead-ends (Fig. 9 in Ref. 2). However, a periodic arrangement with interactions is possible when the dead-end pores are opened into the main pores as shown in Fig. 1. In this case, the interaction between the dead-end and the connected pores occurs in the bulk of the material slab. Only the straight perforations going through the thickness of the material layer are visible on the surface.

When the dead-ends are distributed periodically along the length of the main pores, two distinctive cases can be identified in the material behavior. If the wavelength of

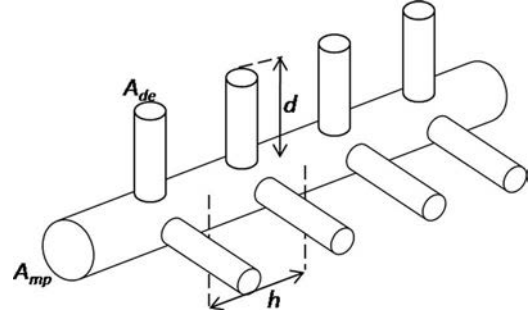


FIG. 1. Main pore (cross-sectional area A_{mp}) with periodically arranged dead-end pores, $N=2$ identical dead-end pores with cross-section area A_{de} and length d per period h . The dead-ends are located at “nodes.”

sound traveling through the main pores is comparable to the distance between the dead-ends, stop and pass bands may appear. However, in the small pores on the order of the viscous and thermal boundary layers thicknesses, these effects will be severely affected by the strong viscous and thermal losses. In the case where the separation distance between the dead-ends is much less than the wavelength, the effective properties of the porous material (i.e., its effective density and compressibility) are modified by their presence. The validity of the plane wave approximation is assumed throughout the paper i.e., the radii of all pores are assumed small compared to the wavelength of sound.

Following Bradley,³ a pore with cross-sectional area A_{mp} (the subscript “ mp ” stands for “main pore”) with periodically distributed identical side branches with cross-sectional area A_{de} (the subscript “ de ” stands for “dead-end”) and length d is considered. There are N dead-ends per period h . A configuration with $N=2$ is shown in Fig. 1. It is assumed that $\text{Re}(k_{mp}\sqrt{A_{mp}}) \ll 1$, $\text{Re}(k_{de}\sqrt{A_{de}}) \ll 1$ so that the wave inside the pores is plane. Here, k_{mp} and k_{de} are the wavenumbers in the main pore and in the dead-ends. The period h can be comparable to the wavelength. In this case, the wavenumber q of Bloch waves (i.e., waves that propagate through a periodic structure) is defined by the following dispersion equation, which is equivalent to Eq. (27) in Ref. 3,

$$\cos(qh) = \cos(k_{mp}h) + iX \sin(k_{mp}h), \quad (1)$$

where

$$X = -\frac{N A_{de}}{2 A_{mp}} \frac{1}{Z_{sde}} \quad (2)$$

in which the number of dead-end pores per node N appears when applying the pressure and volume velocity continuity at the entrance of the junction Ref. 3 (Appendix), Ref. 6 (p. 290). Z_{sde} is the normalized surface impedance of the dead-end. In case of a simple dead-end pore,

$$Z_{sde} = i \frac{Z_{de}}{Z_{mp}} \cotan(k_{de}d) \quad (3)$$

and

$$X = i \frac{N A_{de}}{2 A_{mp}} \frac{Z_{mp}}{Z_{de}} \tan(k_{de}d). \quad (4)$$

Contrary to Ref. 3, the difference between the characteristic impedance of air in the main pore and in the dead-end pore is accounted for in Eqs. (3) and (4). This difference may arise due to the difference in shape or in cross-sectional area of these pores if viscous and thermal losses are present. The side branches of different nature (Helmholtz resonators for instance) can be easily accommodated by using an appropriate surface impedance instead of Eq. (3).

Here Z_{mp} and Z_{de} are the characteristic acoustic impedances of air inside the main pore and in the dead-end pores. A time dependence in the form $\exp(-i\omega t)$ is assumed. It is easy to generalize Eq. (2) for the case of N non-identical dead-end pores per period,

$$X = -\frac{1}{2} \frac{Z_{mp}}{A_{mp}} \sum_{k=1}^N \frac{A_{de}^{(k)}}{Z_{de}^{(k)}} \tan(k_{de}^{(k)} d^{(k)}). \quad (5)$$

In this case, the characteristics of the individual dead-ends are denoted by the superscript (k) . If we define

$$y = \exp(ik_{mp}h), \quad (6)$$

then the following matrix:

$$\mathbf{T}_c = \begin{pmatrix} (1+X)y & X \\ -X & \frac{(1-X)}{y} \end{pmatrix}, \quad (7)$$

relates forward and backward propagating Bloch waves on the right and on the left from the period of size h along the thickness.

If n periods are considered, then forward and backward propagating Bloch waves on the right and on the left from this arrangement are related by the matrix \mathbf{M} ,

$$\mathbf{M} = (\mathbf{T}_c)^n = \begin{pmatrix} M_{11} & M_{12} \\ M_{21} & M_{22} \end{pmatrix}. \quad (8)$$

Now the equation for pressure reflection r_n and transmission t_n coefficients for n periods in an open channel (main pore of Fig. 1 with infinite length so that no reflection occurs outside the dead-end arrangement area) is

$$\begin{pmatrix} t_n \\ 0 \end{pmatrix} = \mathbf{M} \begin{pmatrix} 1 \\ r_n \end{pmatrix}, \quad (9)$$

which gives

$$r_n = -\frac{M_{21}}{M_{22}}, \quad (10a)$$

$$t_n = \frac{1}{M_{22}}. \quad (10b)$$

Here the fact that $\det \mathbf{M} = 1$ (product of matrices bearing the same property) was used. If the reflection coefficient r'_n from a rigidly backed structure containing n unit cells is to be calculated (main pore of Fig. 1 with hard back after the last dead-end), it is given by

$$\begin{pmatrix} P \\ P \end{pmatrix} = \mathbf{M} \begin{pmatrix} 1 \\ r'_n \end{pmatrix}, \quad (11)$$

where P is the amplitude of the incident and reflected waves at the rigid surface. Eliminating P from Eq. (11) results in

$$r'_n = \frac{M_{11} - M_{21}}{M_{22} - M_{12}}. \quad (12)$$

To model the sound interaction with a porous material containing straight pores (of surface perforation rate ϕ) with dead-ends, each pore is associated with an air channel of cross-sectional area A so that

$$\phi = \frac{A_{mp}}{A} \quad (13)$$

as illustrated in Fig. 2. For the plane wave approximation to be valid, it is necessary that $k\sqrt{A_{mp}/\phi} \ll 1$, where $k = \omega/c$ is wavenumber in air and c is the sound speed in air.

Then the amplitudes of the forward and backward traveling waves in the hypothetical channels and at the entrance to the main pores, p'_+ and p'_- , are related by

$$\begin{pmatrix} p'_+ \\ p'_- \end{pmatrix} = \mathbf{T} \begin{pmatrix} p'_+ \\ p'_- \end{pmatrix}, \quad (14)$$

where

$$\mathbf{T} = \begin{pmatrix} \frac{1+\phi'}{2\phi} & -\frac{1-\phi'}{2\phi} \\ -\frac{1-\phi'}{2\phi'} & \frac{1+\phi'}{2\phi'} \end{pmatrix}, \quad (15)$$

where $\phi' = \phi(z_0/Z_{mp})$ and z_0 the characteristic acoustic impedance of air.

This means that the reflection and transmission coefficients of an open ended porous material slab, R_n and T_n and a reflection coefficient R'_n of a hard backed porous slab can be calculated using equations similar to those derived for a

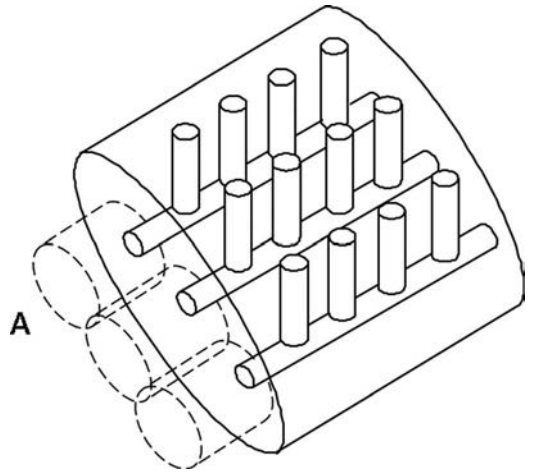


FIG. 2. Modeling transmission and reflection through the material surface. Each pore is associated with an air channel of cross-sectional area A given by Eq. (13).

single pore, Eqs. (10a), (10b), and (12). The former can be calculated by

$$R_n = -\frac{M'_{21}}{M'_{22}}, \quad (16a)$$

$$T_n = \frac{1}{M'_{22}}, \quad (16b)$$

and the latter by

$$R'_n = \frac{M'_{11} - M'_{21}}{M'_{22} - M'_{12}}, \quad (17)$$

where the elements M'_{ij} of a matrix \mathbf{M}' are used. This matrix is given by the product of \mathbf{M} and \mathbf{T} ,

$$\mathbf{M}' = \mathbf{M} \times \mathbf{T}, \quad \mathbf{M} = \mathbf{T}^{-1} \times \mathbf{M}'. \quad (18)$$

The absorption coefficient of a hard backed slab is calculated by

$$\alpha = 1 - |R'_n|^2. \quad (19)$$

III. LOW FREQUENCY APPROXIMATION

Now it is assumed that the distance h between the dead-ends is much less than the wavelength of sound in the main pore, i.e., $\text{Re}(k_{mp}h) \ll 1$. In this case, the configuration with dead-end pores can be replaced by the main pore filled with a fluid described by the effective wavenumber q and the effective impedance z . To derive the expressions for q and z , a simple self-consistent model similar to a coherent potential approximation (CPA) (Ref. 7) is used. In this method the configuration shown in Fig. 1 is replaced by a pore filled with a fluid with still unknown effective properties. Then the following ‘‘gedankenexperiment’’ is performed: If a unit cell of an original periodic arrangement is inserted into this pore, it will not disturb the properties of an effective fluid representing exactly the same periodically arranged unit cells as the inserted one. This implies that if a wave travels through the pore filled with effective fluid, its reflection coefficient from the inserted cell will be 0 and the transmission coefficient will be equal to $\exp(iqh)$. In addition, the implicit assumption that the sample is of infinite length or, at least sufficiently long to include many wavelengths is made. The period insertion is illustrated in Fig. 3.

Assuming no reflections at $x = -h/2$, the boundary conditions for pressure and particle velocity at this location are

$$1 = a_+ e^{(-ik_{mp}h)/2} + a_- e^{(ik_{mp}h)/2}, \quad (20)$$

$$\frac{1}{z} = \frac{1}{Z_{mp}} (a_+ e^{(-ik_{mp}h)/2} - a_- e^{(ik_{mp}h)/2}), \quad (21)$$

where a_{\pm} are the amplitude of the forward and backward waves propagating between $x = -h/2$ and $x = 0$. All quantities are normalized to the amplitude of the incident wave on

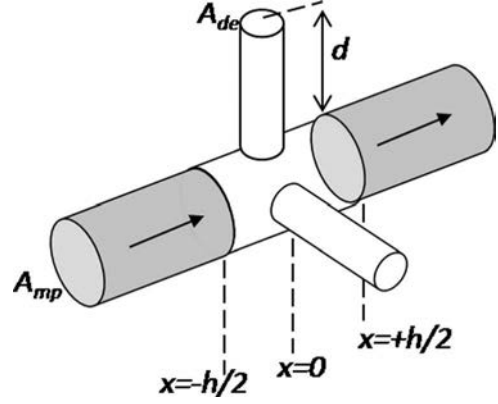


FIG. 3. (Color online) A pore filled with effective fluid and a single unit cell inserted in it. The arrow shows a propagating pressure wave.

the cell from the effective medium. At $x = 0$, the wave amplitude are modified due to the presence of the dead-end pores. Generalizing the transfer matrix derived in Ref. 3 to the case of N identical dead-ends, the amplitudes b_{\pm} of the waves propagating between $x = 0$ and $x = h/2$ can be related to a_{\pm} in the following way:

$$b_+ = a_+(1 + X) + a_-X, \quad (22)$$

$$b_- = -a_+X + a_-(1 - X). \quad (23)$$

Finally, with the transmission coefficient being equal to $\exp(iqh)$, the boundary conditions at $x = h/2$ are

$$e^{iqh} = b_+ e^{(ik_{mp}h)/2} + b_- e^{(-ik_{mp}h)/2}, \quad (24)$$

$$\frac{e^{iqh}}{z} = \frac{1}{Z_{mp}} (b_+ e^{(ik_{mp}h)/2} - b_- e^{(-ik_{mp}h)/2}). \quad (25)$$

Combining Eqs. (20) and (21) provides the ratio a_-/a_+ as a function of z , Z_{mp} , and $k_{mp}h$. Combining Eqs. (22) and (23) provides the ratio b_-/b_+ as a function of a_-/a_+ . The ratio b_-/b_+ is then replaced in the combined Eqs. (24) and (25) to provide

$$\left(\frac{Z_{mp}}{z}\right)^2 = \frac{i \sin(k_{mp}h) + X(\cos(k_{mp}h) + 1)}{i \sin(k_{mp}h) - X(1 - \cos(k_{mp}h))}, \quad (26)$$

$$e^{iqh} = (\cos(k_{mp}h) + iX \sin(k_{mp}h)) + \frac{Z_{mp}}{z} (i \sin(k_{mp}h) - X(1 - \cos(k_{mp}h))). \quad (27)$$

At low frequencies, in a first order expansion over a small parameter $k_{mp}h$, $\cos(k_{mp}h)$ is approximated by 1 and $\sin(k_{mp}h)$ is approximated by $k_{mp}h$ and the following expressions for the characteristic acoustic impedance are obtained:

$$z = \frac{Z_{mp}}{\sqrt{1 + \frac{2X}{ik_{mp}h}}} = \frac{Z_{mp}}{\sqrt{1 + \frac{NA_{de} Z_{mp} \tan(k_{de}d)}{A_{mp} Z_{de} k_{mp}h}}}. \quad (28)$$

For the wavenumber q , the low frequency asymptotic behavior can be determined by an expansion to the second order of

Bradley's dispersion Eq. (1). Alternatively, an expansion of the dispersion Eq. (27) can be considered. Because e^{iqh} contains $\cos(qh)$, the expansion should be done to the second order to achieve the same precision. The method proposed here consists in determining first the real part $\cos(qh)$ and imaginary part $\sin(qh)$ of the exponential. Upon inserting Eq. (26) in Eq. (27), it can easily be shown that

$$e^{iqh} = (\cos(k_{mp}h) + iX \sin(k_{mp}h)) + i\sqrt{1 - (\cos(k_{mp}h) + iX \sin(k_{mp}h))^2}. \quad (29)$$

And consequently since $e^{iqh} = \cos(qh) + i \sin(qh)$, the following split is the only solution:

$$(\cos(k_{mp}h) + iX \sin(k_{mp}h)) = \cos(qh), \quad (30)$$

$$\begin{aligned} i\sqrt{1 - (\cos(k_{mp}h) + iX \sin(k_{mp}h))^2} \\ = \frac{Z_{mp}}{z} (i \sin(k_{mp}h) - X(1 - \cos(k_{mp}h))) \\ = i\sqrt{1 - \cos^2(qh)} = i \sin(qh). \end{aligned} \quad (31)$$

These results show that the present approach ("gedankenexperiment") leads to a dispersion relation [Eq. (27) or (29)] that is equivalent to Eq. (1), and in addition, Eq. (26) provides an expression of the equivalent characteristic impedance z as a function of k_{mp} .

At low frequencies, the wavenumber q of the effective medium can be considered small and is obtained with the help of an expansion to the second order of Eq. (30) or to the first order of Eq. (31), which only involves $\sin(qh)$. The same result is obtained in both cases,

$$q = k_{mp} \sqrt{1 + \frac{2X}{ik_{mp}h}} = k_{mp} \sqrt{1 + \frac{NA_{de} Z_{mp} \tan(k_{de}d)}{A_{mp} Z_{de} k_{mp}h}}. \quad (32)$$

It is now possible to obtain expressions for the effective density $\rho_e = zq/\omega$ and for the effective compressibility $C_e = q/(z\omega)$ of the fluid in the pore with dead-ends,

$$\rho_e = \rho_{mp}, \quad (33)$$

$$C_e = C_{mp} + C_{de} \frac{NA_{de} d}{A_{mp} h} \left(\frac{\tan(k_{de}d)}{k_{de}d} \right), \quad (34)$$

where $\rho_{mp} = Z_{mp}k_{mp}/\omega$ and $C_{mp} = k_{mp}/\omega Z_{mp}$ are the effective density and compressibility of the fluid in the main pore and $C_{de} = k_{de}/\omega Z_{de}$ is the compressibility of the fluid in the dead-end pores. It follows from Eq. (33) that the presence of the dead-end pores does not affect the effective density of the fluid in the main pore at low frequencies. However, it could significantly modify its effective compressibility. Now, Eqs. (28) and (32) are conveniently rewritten as

$$z = \sqrt{\frac{\rho_e}{C_e}} = \sqrt{\frac{\rho_{mp}}{C_{mp} + C_{de} \frac{NA_{de} d}{A_{mp} h} \left(\frac{\tan(k_{de}d)}{k_{de}d} \right)}}, \quad (35)$$

$$\begin{aligned} q &= \omega \sqrt{\rho_e C_e} \\ &= \omega \sqrt{\rho_{mp} \left(C_{mp} + C_{de} \frac{NA_{de} d}{A_{mp} h} \left(\frac{\tan(k_{de}d)}{k_{de}d} \right) \right)}. \end{aligned} \quad (36)$$

The characteristic impedance z_m of the material with perforation rate ϕ can be calculated from Eq. (35) as

$$z_m = \frac{z}{\phi} = \frac{1}{\phi} \sqrt{\frac{\rho_{mp}}{C_{mp} + C_{de} \frac{NA_{de} d}{A_{mp} h} \left(\frac{\tan(k_{de}d)}{k_{de}d} \right)}}, \quad (37)$$

and the wavenumber is defined by Eq. (36).

The dependence of ρ_{mp} , ρ_{de} and C_{mp} , C_{de} on frequency and radius of both types of pores can be described by classical theories of wave propagation in cylindrical tubes (see Ref. 1, Chap. 4 for a review and description of these theories). The cylindrical pores can also be described using general models of wave propagation in porous media such as the Attenborough model⁸ or the Johnson, Koplik, Dashen model⁹ with macroscopic parameters corresponding to cylindrical pore structure. These models are generalized by Champoux and Allard¹⁰ to account for thermal effects. To make our results easy to generalize to other pore geometries, models of porous materials, the models by Johnson *et al.* and by Champoux-Allard (synthesized in the "JCA model") are used to describe sound propagation in both main and dead-end pores. The following expressions are used for the effective density and compressibility of fluid in the main and dead-end pores (subscripts "de" and "mp" are omitted in the following two equations):

$$\rho = \rho_0 \alpha_\infty \left(1 + \frac{\sigma}{-i\omega \alpha_\infty \rho_0} \sqrt{1 + \frac{-i\omega}{\omega_b}} \right), \quad (38)$$

$$C = \frac{1}{\rho_0 c^2} \left(\gamma - \frac{\gamma - 1}{1 + \frac{\eta}{-i\omega' \rho_0 \kappa'} \sqrt{1 + \frac{-i\omega'}{\omega'_b}}} \right), \quad (39)$$

with $\omega' = \omega \sqrt{N_{pr}}$, $\omega_b = \sigma^2 \Lambda^2 / (4\alpha_\infty^2 \rho_0 \eta)$, and $\omega'_b = \Lambda'^2 / (4\kappa'^2 \rho_0)$ where N_{pr} is the Prandtl number, σ the air-flow resistivity, Λ the viscous characteristic length, α_∞ the tortuosity, ρ_0 the air density, η the dynamic viscosity, Λ' the thermal characteristic length and κ' the thermal permeability which is a parameter defined in the model by Lafarge *et al.*¹¹ Here σ and κ' are parameters of a single pore and not of the bulk material. Different pore geometries can be accounted for by choosing different sets of parameters in the JCA model. For circular cross-section uniform cylinder, Λ and Λ' are equal to the pore radius. In the calculations presented in Sec. IV, the main pore and the dead-ends are supposed to be straight and cylindrical and so the data displayed in Table I are used.

If the slab is hard backed and its thickness is L , then its surface impedance is calculated as

$$z_s = iz_m \cotan(qL), \quad (40)$$

and the absorption coefficient is

$$\alpha = 1 - \left| \frac{z_s - z_0}{z_s + z_0} \right|^2. \quad (41)$$

IV. SINGLE MAIN PORE WITH LATERAL DEAD-ENDS: MODEL PREDICTIONS AND LIMITATIONS OF THE LOW FREQUENCY APPROXIMATION

In this section, the comparisons between the full analytical TMM model accounting for periodicity in the arrangement of the dead-ends and the low frequency approximation are presented. The limitations of the latter are identified.

A. Cylindrical pore with long lateral dead-ends

First, a single cylindrical pore with lateral dead-ends is considered to study the limitations of the low frequency approximation. Identical dead-end pores with length $d = 3$ cm are assumed distributed along the main pore with a period $h = 1$ cm. The radius of the main pore is $a_{mp} = 3$ mm and the radius of dead-end pore is $a_{de} = 1$ mm, $N = 8$ lateral dead-ends per period are considered. First, real and imaginary parts of the wavenumber q defined by (1) are calculated and compared to those predicted by a low frequency approximation [Eq. (32)]. The frequency range is chosen so that $\text{Re}(k_{mp})a_{mp} \leq 0.5$ to justify the use of a plane wave approximation.

Two resonances of dead-ends [$\text{Re}(k_{de})d = \pi/2$ and $\text{Re}(k_{de})d = 3\pi/2$] are observed at frequencies 2709 Hz and 8200 Hz. These resonances are well below the Bragg frequency (17 241 Hz), which is outside the range where the plane wave approximation is valid. The low frequency model [Eq. (32)] accurately predicts the frequency of the first resonance, while overestimating both real and imaginary parts of the wavenumber at the resonance due to strong dispersion. As for the second resonance, the low frequency model slightly overestimates its frequency (within 2% error) and lacks accuracy around it. Figure 5 compares the low frequency model predictions for the absorption coefficient predictions of a single hard backed pore of two different lengths.

Two lengths of the main pore ($L = 2$ cm and $L = 5$ cm) are considered. The first length corresponds to two elementary cells per length, while the second corresponds to five. In both cases, resonances of the dead-ends correspond to the maxima in the absorption coefficient dependence on frequency. However, the behavior around the resonances of the dead-ends is distorted by the quarter-wavelength resonances

TABLE I. Parameters of Johnson-Champoux-Allard and of Lafarge *et al.* model (Ref. 11) for straight cylindrical pores (subscript *mp*) and dead-ends (subscript *de*).

$\sigma_{mp,de}$	$\kappa'_{mp,de}$	$\alpha_{\infty,mp,de}$	$\Lambda_{mp,de}$	$\Lambda'_{mp,de}$
$8\eta \backslash a_{mp,de}^2$	$a_{mp,de}^2 / 8$	1	$a_{mp,de}$	$a_{mp,de}$

of the hard-backed pore. These resonances happen roughly when $\text{Re}(q)L = \pi/2$. Due to strongly dispersive behavior of the resonance modes as shown in Fig. 4, multiple quarter wavelength resonances of the structure occur in the frequency range considered. So for $L = 2$ cm [Fig. 5(a)] $\text{Re}(q)L = \pi/2$ at 1820, 4900, and 8360 Hz. Low frequency model predicts reasonably accurately the absorption coefficient behavior around the first resonance of the dead-ends, while it becomes inaccurate and not able to resolve the interaction between the resonances of the dead-ends and those of the hard backed structure at higher frequencies. The absorption coefficient of the cylindrical main pore without dead-ends is shown in both Figs. 5(a) and 5(b) to illustrate a significant increase in absorption due to the presence of dead-ends.

B. Main pores with short lateral dead-ends

It follows from the expression for the effective compressibility [Eq. (34)] that if the length of dead-ends is much shorter than the wavelength $\text{Re}(k_{de}d) \ll 1$, the effective compressibility is approximated as

$$C_e = C_{mp} + C_{de} \frac{V_{de}}{V_{mp}}, \quad (42)$$

where $V_{de} = NA_{de}d$ and $V_{mp} = A_{mp}h$ are volumes of the dead-ends and the main pore portion per period h of the structure. This means that a significant decrease in the phase velocity of sound through the pore could be achieved if the total volume of dead-ends per period significantly exceeds

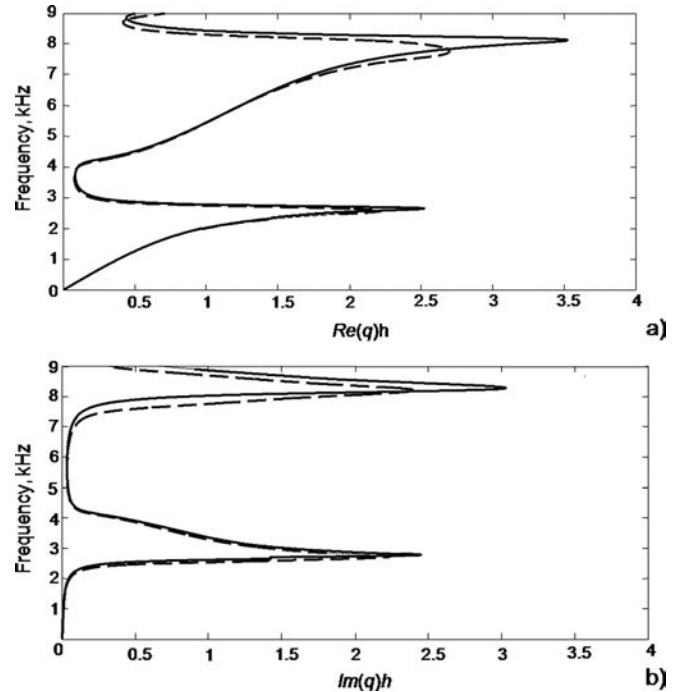


FIG. 4. Comparisons of the real (a) and imaginary (b) parts of the normalized wavenumber in main pore with long lateral dead-ends predicted by the analytical TMM model and the low frequency approximation. Dashed line, analytical TMM model (1); solid line, low frequency approximation (32), $N = 8$ identical lateral dead-ends of length $d = 3$ cm per period $h = 1$ cm, dead-end radius $a_{de} = 1$ mm, and main pore radius $a_{mp} = 3$ mm.

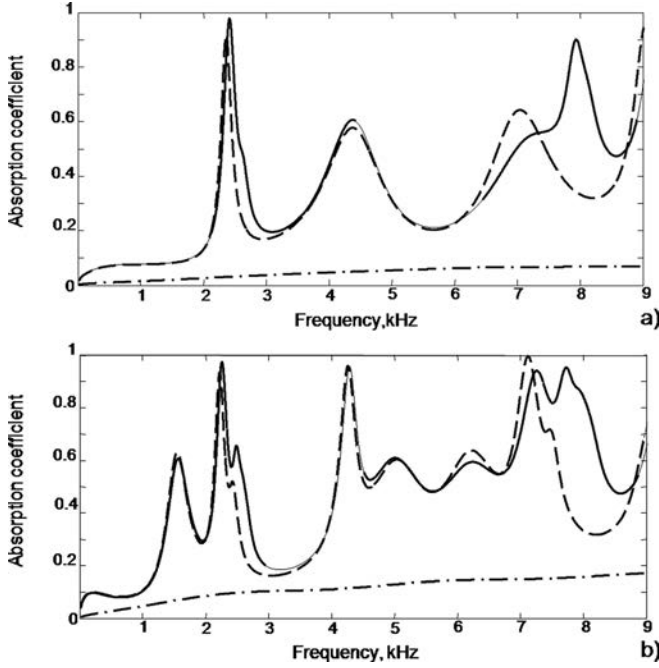


FIG. 5. Absorption coefficient of the single hard backed main pore with long lateral dead-ends as a function of frequency. (a) Main pore length $L=2$ cm, (b) main pore length $L=5$ cm. Dashed line, analytical TMM model [Eq. (19)]; solid line, low frequency approximation [Eq. (41)]; and dashed-dotted line, main pore with no dead-ends. Parameters as in Fig. 4.

that of the main pore. Assuming that the radii of the dead-ends and the main pore are fixed, this could be achieved by (a) increasing the length d of the dead-ends, (b) increasing the number of dead-ends N per period, and (c) decreasing the period h , i.e., spacing the dead-ends closer to each other. Sound speed in the pore with lateral dead-ends of length $d=3$ mm normalized to sound speed in air is shown in Fig. 6(a) for two periods $h=1$ cm and $h=3$ mm. Normalized sound speed in main pore without dead-ends is shown for comparison. As in the previous calculations, the radius of the main pore is $a_{mp}=3$ mm and the radius of dead-end pore is $a_{de}=1$ mm. Again, $N=8$ lateral dead-ends per period are considered. In the frequency range below 9 kHz, no resonances of the dead-ends are observed. The lowest resonance frequency corresponding to $\text{Re}(k_{de})d = \pi/2$ is 22 000 Hz. The lowest Bragg frequency (for $h=1$ cm) is 17 241 Hz, which is also outside the frequency range considered. For this value of the period, the disagreement between the low frequency and the full analytical TMM model predictions for sound speed become noticeable at around 4000 Hz, which corresponds to $|k_{mp}|h \approx 0.7$. For a shorter period $h=3$ mm, the low frequency model predictions remain accurate in the whole frequency range. Absorption coefficient predictions for a hard backed pore with length $L=5$ cm are shown in Fig. 6(b).

The absorption coefficient of the structure with dead-ends significantly exceeds that of the cylindrical main pore, especially when the dead-ends are closely spaced ($h=3$ mm) and consequently a significant reduction in sound speed is achieved. The absorption coefficient dependence in this case shows multiple peaks due to quarter-wavelength resonances of the structure.

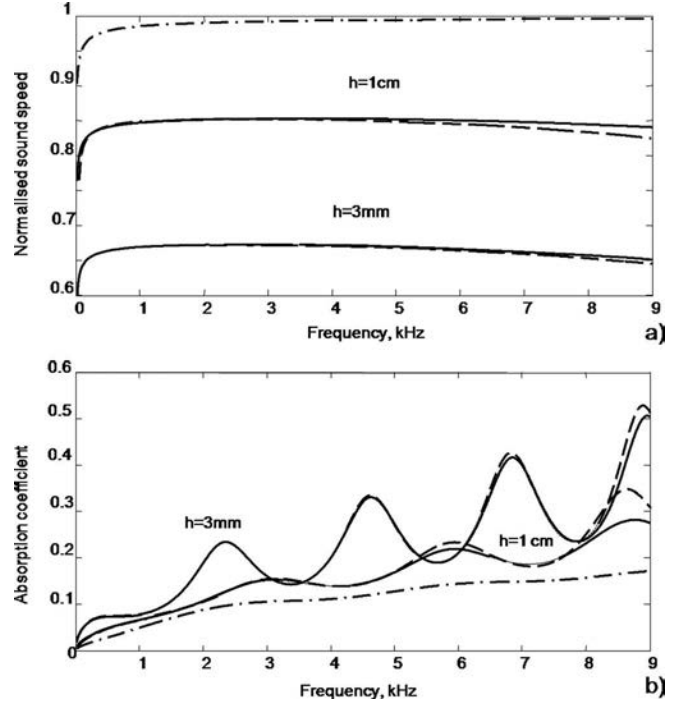


FIG. 6. Normalized sound speed (a) and absorption coefficient (b) of a single main pore with short lateral dead-ends as a function of frequency. Predictions for periods $h=3$ mm and $h=1$ cm are shown. Legend as in Fig. 5. Parameters as in Fig. 4 except that dead-end length is $d=3$ mm. Absorption coefficient is calculated for a hard backed pore with length $L=5$ cm.

V. MODEL VALIDATION

A. Comparison between different approaches

Comparisons among the present analytical model, transfer matrix approach (TMM), and virtual measurements obtained with a 3D acoustical FEM simulations using COMSOL software have been performed. A three microphones method¹² is used to get the virtual FEM measurements. In the FEM model on COMSOL, parabolic tetrahedral elements were used to mesh the different domains of the tube and an effective fluid of density and bulk modulus given by the JCA model^{9,10} fills the pores.

In the FEM simulations (Fig. 7), several aspects have been considered to optimize the precision and computation time: A sufficient number of elements per domain to be meshed has been chosen in order to ensure a good precision while keeping the computation time minimum, an adaptive mesh has been used with increased number of elements in the vicinity of geometrical discontinuities or in smaller domains (with respect to other domains), sufficiently smooth variations were considered in the mesh element sizes in the vicinity of geometrical discontinuities and domains size variations. In addition, it was made sure that a sufficient spatial sampling was considered with respect to the domain discretized. A criterion of one-tenth of the minimum wavelength corresponding to a maximum frequency of 5 kHz was used to choose the minimum size of the meshing elements. In consideration of these requirements, typical values of 20 000 elements per meshed domains were used. The convergence was also verified by varying the meshing

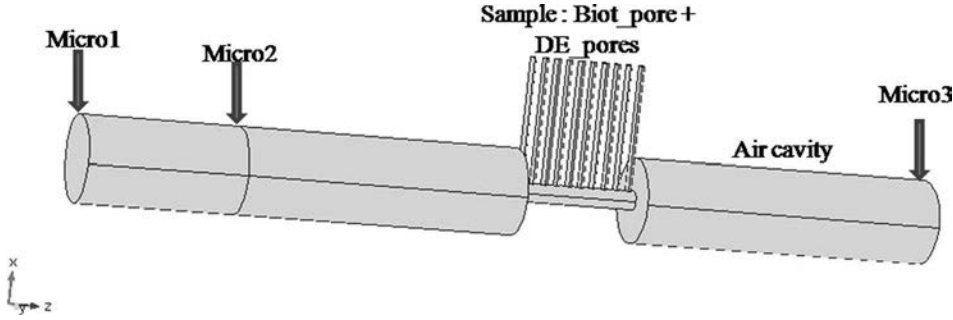


FIG. 7. (Color online) Configuration used in the FEM simulation (virtual FEM measurement). The material parameters are as follows: $L=20$ mm; $a_{mp}=0.5$ mm; $a_{de}=0.5$ mm, $d=19.5$ mm, $\phi=5\%$, $N=1$, and $h=2$ mm. The DE pores are in aligned configuration.

parameters and by making sure the chosen convergence criterion was met in each case.

At low frequency, the FEM simulation confirms the predictions of the analytical TMM model and the low frequency approximation (see Fig. 8). The small discrepancy between TMM and FEM observed above 3500 Hz might be due to the sound radiation end effects at the junctions between main pores and dead-ends. Another possible reason could be the breaking of the validity of the plane wave approximation that requires the distances between the main pores to be much less than the wavelength to discard sound diffusion effects.

B. Comparison with experimental results for a sample obtained from 3D printing

Experimental results on 3D printed materials with dead-end pores (MP50) studied by Dupont *et al.*¹³ were compared with the model. This sample was built using 3D printing technology. The sample shown in Fig. 9 has four types of pores. The pore characteristics are listed in Table II. The overall perforation rate of the sample is $\phi = 23.4\%$.

For this sample, the TMM model described in Sec. II has been modified to account for the three types of dead-end pores and for pores without dead-ends. Equation (16) has been used to calculate pressure reflection coefficient in the channel associated with each pore as shown in Fig. 2. A uniform distribution of pores at the material surface was assumed. Due to this, the overall perforation rate of the sample was used to calculate the surface area A of the channels [see Eq. (13)]. After that, the pressure was averaged across

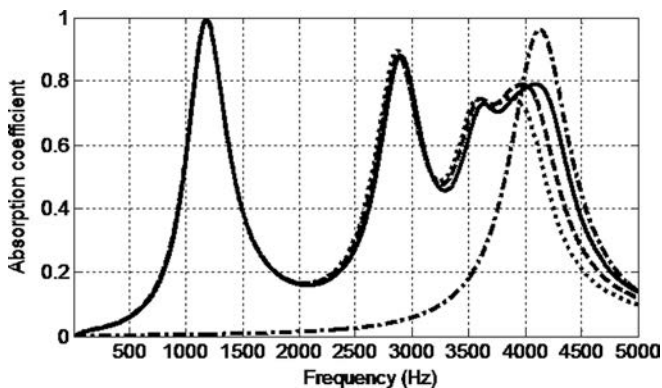


FIG. 8. Absorption coefficient calculated for the configuration shown in Fig. 7. Dashed line, analytical TMM model [Eq. (19)]; solid line, low frequency approximation [Eq. (41)]; dashed-dotted line, main pore with dead-ends (analytical model); and dotted line, FEM simulation.

the surface of the sample. The comparison between the measurements and the model predictions for the absorption coefficient is shown in Fig. 10(a).

The experimental curve was obtained by averaging three sets of results obtained from measurements at different times on three identically designed samples in repeatability experiments. The simulation accounts for the end correction of the main pores, which corresponds to a tortuosity correction because the stream lines at the entry face and exit face of the sample are not straight, especially for low perforation rates.¹⁴ The predicted absorption peak is due to the presence of dead-ends. The predicted resonance is broader than the observed one. It is thought that this is due to the fact that the dead-ends in the fabricated sample are slightly thinner than expected in the material design. The 3D printing process uses a powder the particles of which are glued together with the help of a liquid binder. Successive layer are bound together to form the 3D structure. The structure is then heated so that the binder is evaporated, and the particles of the powder sintered. This process leaves a microporosity. To remove the influence of this microporosity, the sample including the dead-end pores has been covered by a varnish that may have reduced the pore diameter. Measuring with precision the actual diameter of the dead-end pores on the fabricated 3D sample is currently a difficult task. The error in the 3D printing process is estimated to be 0.01 mm for a sample of a few centimeter thickness. A simulation using a smaller diameter for the dead-end pores shows that the absorption peak is narrowed as expected. This provides an indirect confirmation that the pores are thinner than expected. Because the reduction in pores diameter is difficult to measure with precision, only the results with the nominal desired diameter are shown in Fig. 10.

The discrepancy above 3000 Hz might be due to microporosity of the sample created in the 3D printing process. However, the low frequency match is fairly good. For the transmission loss, it is noticed that the presence of the dead-ends removes the anti resonance (dip) predicted when the sample thickness (the main pore length) is half the wavelength. This can be explained by the fact that the dead-ends render the effective fluid more compressible and slow down the wave so as to shift the anti resonance to lower frequencies. In addition, the distribution in dead-end lengths will have the effect of reducing the quality factor of the anti resonance and of making the transmission loss smoother. The theoretical and experimental results in Fig. 10 seem to confirm these remarks.

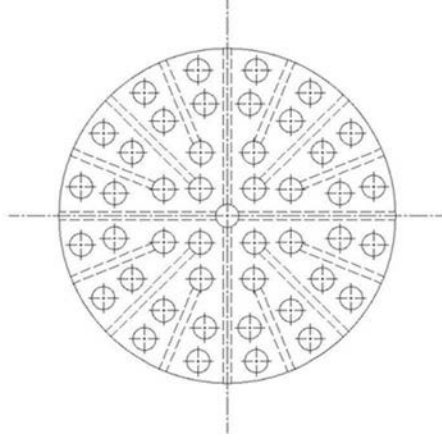
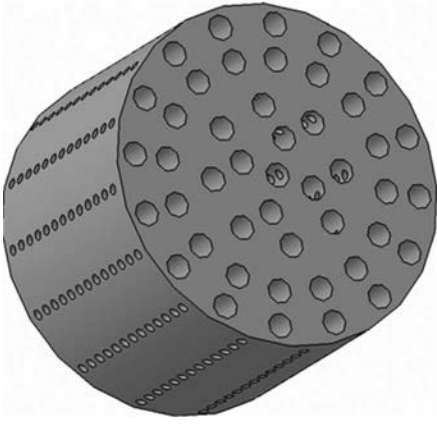


FIG. 9. A porous sample with dead-ends (after sealing the circumference) used in the measurements. The sample diameter is 44.4 mm, and its thickness is $L = 30$ mm.

With the help of the model developed in this work and with the TMM or FEM simulations, it is now possible to design structures giving larger shifts of the absorption coefficient peak toward low frequencies if the Main/DE pores parameters are properly chosen. This opens up new experimental possibilities for future work.

VI. POSSIBLE DESIGNS AND NUMERICAL SIMULATIONS

In this section, materials designs involving periodically spaced dead-ends in the thickness are proposed. Equation (42) provides a tool in the first steps toward the design of high performance materials at low frequencies using periodic dead-end pores. The underlying idea is to increase the compressibility at low frequency C_e of the equivalent fluid, which can be rewritten

$$C_e = C_{mp} + C_{de} \left(\frac{a_{de}}{a_{mp}} \right)^2 \frac{Nd}{h}. \quad (43)$$

At constant pore radii, the compressibility can be increased by increasing the number of dead-ends per node N and by reducing the period h . This last condition is compatible with small thickness requirements in the material design. C_e can be increased by increasing the length d . However, d must remain much smaller than the wavelength for Eq. (43) to remain valid.

TABLE II. Pore characteristics of the four types of pores of the sample presented in Fig. 9.

Pore characteristics	Units	Types of pores			
		1	2	3	4
Number of main pores		1	4	8	32
Porosity of main pores	%	0.52	2.08	4.16	16.62
a_{mp} (Radius of main pores)	mm	1.6	1.6	1.6	1.6
h (DE period)	mm	2.3	2.3	2.3	–
N (DE pores per node)		4	1	1	–
a_{de} (Radius of DE pores)	mm	0.65	0.65	0.65	–
d (Length of DE pores)	mm	20.4	15.4	11.4	–

Examples of possible designs are proposed, one with square perforation design (see Fig. 11) with four dead-ends per node and one with eight dead-ends per node (Fig. 12). The length, sizes of the main pores and dead-ends, the perforation rate can be varied to obtain best performance, especially at low frequencies. The perforation rate can be adjusted with the help of additional perforations without dead-ends. In the following simulations, the frequency range of calculations is chosen so that $\text{Re}[k] \sqrt{A_{mp}/\pi\phi} \leq 0.5$ to justify the use of plane wave models.

In addition to the sizes of the main pores and of the dead-ends, the criteria for the design are that the material

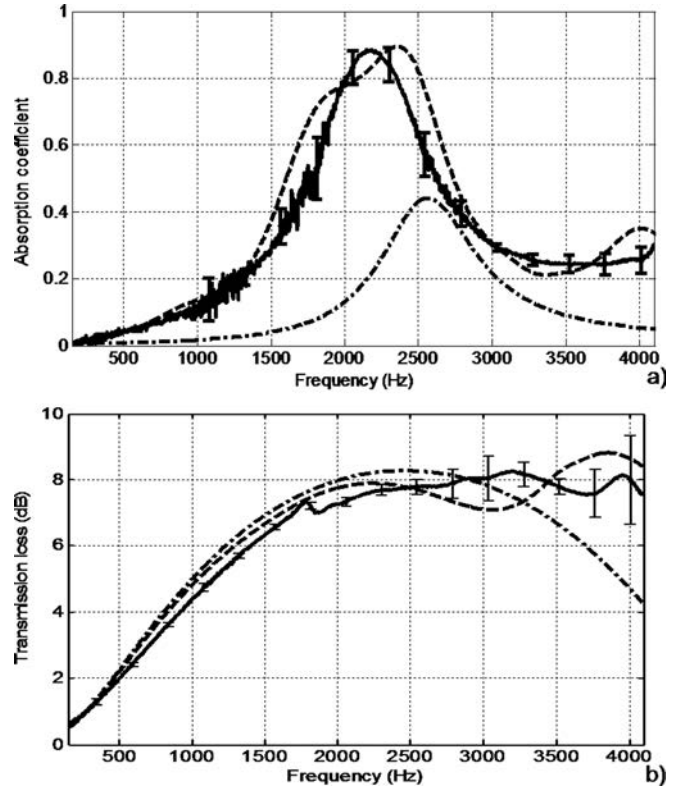


FIG. 10. Experimental results (curve averaged over three repeatability measurements) on (a) the absorption coefficient and (b) on the transmission loss for the MP50 sample (Fig. 9) and comparison between experimental results (plain) and TMM predictions (dashed line). The dashed-dotted curve shows model predictions for the material without dead-ends.

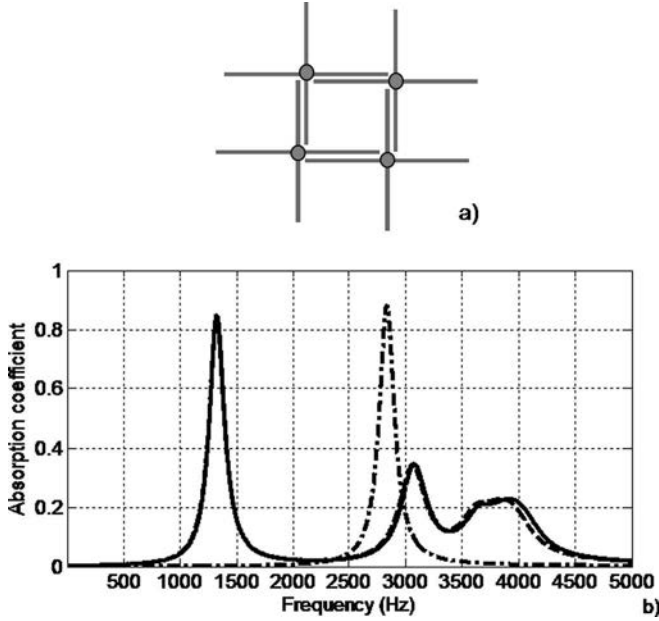


FIG. 11. (Color online) (a) Example of possible design for the front face of a perforated material with lateral dead-ends and (b) simulated results. In this example, $N=4$, $a_{mp}=1.5$ mm, $a_{de}=0.5$ mm, $d=2$ cm, $h=3$ mm, slab thickness $L=3$ cm, perforation rate: $\phi=1.69\%$. Plain curve, low frequency approximation; dashed line, analytical TMM model; and dashed-dotted line, main pores without dead-ends.

should contain as many dead-ends per nodes as possible while the perforation rate corresponding to the main pores should be chosen optimal. The number of nodes is also important and this parameter indirectly dictates the possible material thickness. Despite the low perforation rate, both materials are efficient absorbers of low frequency sound.

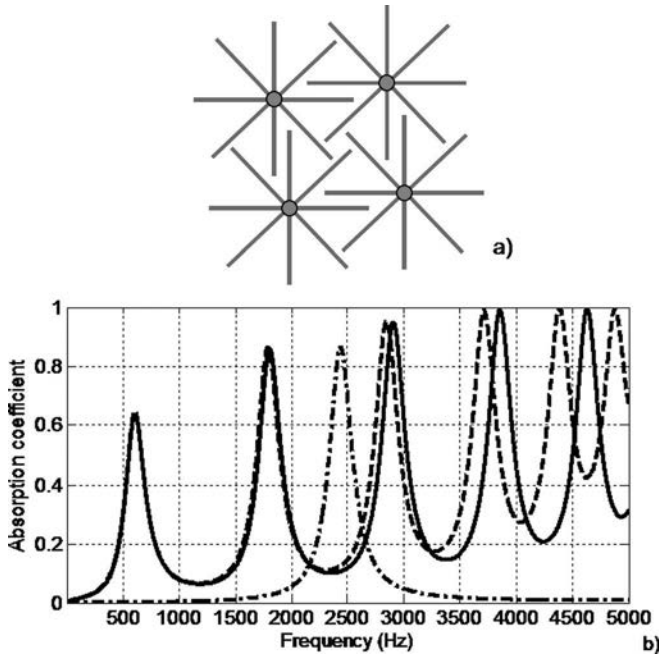


FIG. 12. (Color online) (a) Example of possible design for the front face of a perforated material with lateral dead-ends and (b) simulated results. In this example, $N=8$, $a_{mp}=2$ mm, $a_{de}=1.5$ mm, $d=1$ cm, $h=3.5$ mm, slab thickness $L=3.5$ cm, perforation rate: $\phi=5.39\%$. Plain curve, low frequency approximation; dashed line, analytical TMM model; and dashed-dotted line, main pores without dead-ends.

Future more refined optimization work could include a_{de} and a_{mp} , i.e., the pore radii as additional design parameters. However, because a_{de} and a_{mp} are related to the viscous length and thermal characteristic lengths of the dead-ends and of the main pores, respectively, they also act in C_{de} and in C_{mp} and using them as additional tuning parameters is not as straightforward as for the other parameters. Their influence could be studied in an advanced optimization scheme only.

VII. CONCLUSION

A model for the wave propagation in straight pores with lateral periodically spaced dead-ends is proposed in this work. A low frequency limit of the model is used to derive effective properties of the porous material within this microstructure. The model predicts the possibility of a strong low frequency sound absorption achieved by thin (only a few centimeters) material slabs.

A significant decrease in sound speed in the main pore is predicted at low frequencies. In turn, this low sound speed is responsible for the increase in absorption coefficient well below the frequency predicted by the sole resonance of the dead-ends. The decrease in sound speed may not only be achieved by increasing the length of the dead-ends but also by their number per node or by decreasing the spacing between them [Eq. (43)]. The decrease in sound speed results from the changes in effective compressibility of the fluid in the pores due to the presence of dead-ends while the effective density is not affected [Eqs. (33) and (34)]. This suggests that the mentioned increase in absorption coefficient at low frequencies is the result of thermal exchanges between the fluids filling the main pores and the dead-ends.

The predicted absorption coefficient and transmission loss are compared to the full transfer matrix model and to FEM COMSOL simulations. Experimental results on 3D printed materials are also used to validate the model. Low frequency absorption peaks were observed for a fairly thin sample in accordance with the model predictions.

The model reported in this study provides a simple and efficient tool that can be used in the design of thin low frequency porous absorbers with low surface perforation rate.

ACKNOWLEDGMENTS

The authors wish to thank Université de Bourgogne, France, for financial support in this study.

- ¹J. F. Allard and N. Atalla, *Propagation of Sound in Porous Media: Modelling Sound Absorbing Materials*, 2nd ed. (Wiley and Sons, Chichester, UK, 2009), 372 pp.
- ²T. Dupont, P. Leclaire, O. Sicot, X. L. Gong, and R. Panneton, "Acoustic properties of air-saturated porous materials containing dead-end porosity," *J. Appl. Phys.* **110**, 094903 (2011).
- ³C. E. Bradley, "Time harmonic Bloch wave propagation in periodic waveguides. Part I. Theory," *J. Acoust. Soc. Am.* **96**, 1844–1853 (1994).
- ⁴N. Sugimoto and T. Horioka, "Dispersion characteristics of sound waves in a tunnel with an array of Helmholtz resonators," *J. Acoust. Soc. Am.* **97**, 1446–1459 (1995).
- ⁵X. Wang and C. M. Mak, "Wave propagation in a duct with a periodic Helmholtz resonators array," *J. Acoust. Soc. Am.* **131**, 1172–1182 (2012).

- ⁶L. E. Kinsler, A. R. Frey, A. B. Coppens, and J. V. Sanders, *Fundamentals of Acoustics* (Wiley and Sons, New York, 2000), p. 290.
- ⁷P. Sheng, *Introduction to Wave Scattering, Localization and Mesoscopic Phenomena* (Springer, Berlin, 2006), p. 61.
- ⁸K. Attenborough, "Acoustical characteristics of porous materials," *Phys. Rep.* **82**, 179–227 (1982).
- ⁹D. L. Johnson, J. Koplik, and R. Dashen, "Theory of dynamic permeability and tortuosity in fluid-saturated porous media," *J. Fluid. Mech.* **176**, 379–402 (1987).
- ¹⁰Y. Champoux and J. F. Allard, "Dynamic tortuosity and bulk modulus in air-saturated porous media," *J. Appl. Phys.* **70**, 1975–1979 (1991).
- ¹¹D. Lafarge, P. Lemarinier, J. F. Allard, and V. Tarnow, "Dynamic compressibility of air in porous structures at audible frequencies," *J. Acoust. Soc. Am.* **102**, 1995–2006 (1997).
- ¹²Y. Salissou, O. Doutres, and R. Panneton, "Complement to standard method for measuring normal incidence with three microphones," *J. Acoust. Soc. Am.* **131**, EL216–EL222 (2012).
- ¹³T. Dupont, P. Leclaire, and R. Panneton, "Acoustic methods for measuring the porosities of porous materials incorporating dead-end pores," *J. Acoust. Soc. Am.* **133**, 2136–2145 (2013).
- ¹⁴N. Attala and F. Sgard, "Modeling of perforated plates and screens using rigid frame porous models," *J. Sound Vib.* **303**, 195–208 (2007).